

# Effects of deficiency in the *RLBP1*-encoded visual cycle protein CRALBP on visual dysfunction in humans and mice

Received for publication, January 16, 2020, and in revised form, March 4, 2020. Published, Papers in Press, March 18, 2020, DOI 10.1074/jbc.RA120.012695

Jose Ronaldo Lima de Carvalho Jr.<sup>‡1</sup>, Hye Jin Kim<sup>‡1</sup>,  Keiko Ueda<sup>‡</sup>,  Jin Zhao<sup>‡</sup>, Aaron P. Owji<sup>§</sup>,  Tingting Yang<sup>‡</sup>, Stephen H. Tsang<sup>‡¶1</sup>, and Janet R. Sparrow<sup>‡¶1,2</sup>

From the Departments of <sup>‡</sup>Ophthalmology, <sup>§</sup>Pharmacology, and <sup>¶</sup>Pathology and Cell Biology, Columbia University Irving Medical Center, New York, New York 10032

Edited by Dennis R. Voelker

Mutations in *retinaldehyde-binding protein 1 (RLBP1)*, encoding the visual cycle protein cellular retinaldehyde-binding protein (CRALBP), cause an autosomal recessive form of retinal degeneration. By binding to 11-*cis*-retinoid, CRALBP augments the isomerase activity of retinoid isomerohydrolase RPE65 (RPE65) and facilitates 11-*cis*-retinol oxidation to 11-*cis*-retinal. CRALBP also maintains the 11-*cis* configuration and protects against unwanted retinaldehyde activity. Studying a sibling pair that is compound heterozygous for mutations in *RLBP1*/CRALBP, here we expand the phenotype of affected individuals, elucidate a previously unreported phenotype in *RLBP1*/CRALBP carriers, and demonstrate consistencies between the affected individuals and *Rlbp1*/Cralbp<sup>-/-</sup> mice. In the *RLBP1*/CRALBP-affected individuals, nonrecordable rod-specific electroretinogram traces were recovered after prolonged dark adaptation. In ultrawide-field fundus images, we observed radially arranged puncta typical of *RLBP1*/CRALBP-associated disease. Spectral domain-optical coherence tomography (SD-OCT) revealed hyperreflective aberrations within photoreceptor-associated bands. In short-wavelength fundus autofluorescence (SW-AF) images, speckled hyperautofluorescence and mottling indicated macular involvement. In both the affected individuals and their asymptomatic carrier parents, reduced SW-AF intensities, measured as quantitative fundus autofluorescence (qAF), indicated chronic impairment in 11-*cis*-retinal availability and provided information on mutation severity. Hypertransmission of the SD-OCT signal into the choroid together with decreased near-infrared autofluorescence (NIR-AF) provided evidence for retinal pigment epithelial cell (RPE) involvement. In *Rlbp1*/Cralbp<sup>-/-</sup> mice, reduced 11-*cis*-retinal levels, qAF and NIR-AF intensities, and photoreceptor loss were consistent with the clinical presentation of the affected siblings. These findings indicate that *RLBP1* mutations are associated

with progressive disease involving RPE atrophy and photoreceptor cell degeneration. In asymptomatic carriers, qAF disclosed previously undetected visual cycle deficiency.

Vision is initiated by the absorption of a photon of light by the opsin chromophore 11-*cis*-retinaldehyde in the outer segments of rod and cone photoreceptor cells. This photon capture causes isomerization of 11-*cis*-retinaldehyde to the bleached product all-*trans*-retinaldehyde. For continued light detection, a supply of 11-*cis*-retinal is provided to rod and cone photoreceptor cells by a multistep enzyme pathway, the visual cycle (retinoid cycle), that reconverts all-*trans*-retinal to light-sensitive 11-*cis*-retinal. Cellular retinaldehyde-binding protein (CRALBP),<sup>3</sup> a 36-kDa aqueous soluble carrier, participates in this process (1). CRALBP is expressed in abundance by both retinal pigment epithelial (RPE) and Muller cells of retina and is important for rod- and cone-driven vision (2).

In humans, mutations in *retinaldehyde-binding protein 1 (RLBP1)*, the gene encoding CRALBP, cause autosomal recessive retinal diseases with phenotypes described as retinitis punctata albescens (RPA), autosomal recessive retinitis pigmentosa (arRP), Bothnia dystrophy, and Newfoundland rod-cone dystrophy (2–9). The variable presentation likely reflects, at least in part, the effect of particular mutations on protein structure and function (8). The *RLBP1*/CRALBP phenotype is characterized by varying degrees of early onset delayed dark adaptation, abnormal electroretinographic (ERG) responses, loss of peripheral vision, and progressive macular atrophy (10, 11). Also a characteristic of CRALBP deficiency is the presence of white dot-like aberrations within the fundus (11, 12); these puncta are visible in color fundus and short-wavelength fundus autofluorescence (SW-AF) images (11, 12). RPE atrophy is accompanied by hypertransmission of the spectral domain optical coherence tomography (SD-OCT) signal into the choroid (10). It is esti-

This work was supported by National Institutes of Health Grants EY024091 and EY012951, P30EY019007, and GM127652 and a grant from Research to Prevent Blindness to the Department of Ophthalmology, Columbia University. The authors declare that they have no conflicts of interest with the contents of this article. The content is solely the responsibility of the authors and does not necessarily represent the official views of the National Institutes of Health.

 Author's Choice—Final version open access under the terms of the Creative Commons CC-BY license.

<sup>1</sup> These authors contributed equally to this work.

<sup>2</sup> To whom should be addressed: Dept. of Ophthalmology, Columbia University, 635 W. 165th St., New York, NY 10032. Tel.: 212-305-9944; E-mail: jrs88@columbia.edu.

<sup>3</sup> The abbreviations used are: CRALBP, cellular retinaldehyde-binding protein; cSLO, confocal laser scanning ophthalmoscopy; fERG, full-field electroretinography; NIR-AF, near-infrared fundus autofluorescence; ONL, outer nuclear layer; RDH5, retinol dehydrogenase 5; RLBP1, retinaldehyde-binding protein 1; RPA, retinitis punctata albescens; RPE, retinal pigment epithelium; SD-OCT, spectral domain-optical coherence tomography; SW-AF, short-wavelength fundus autofluorescence; UWF, ultrawide-field; qAF, quantitative fundus autofluorescence; UPLC, ultra-performance LC; ANOVA, analysis of variance; ONH, optic nerve head; Rt, retention time.

## RLBP1/CRALBP gene deficiency

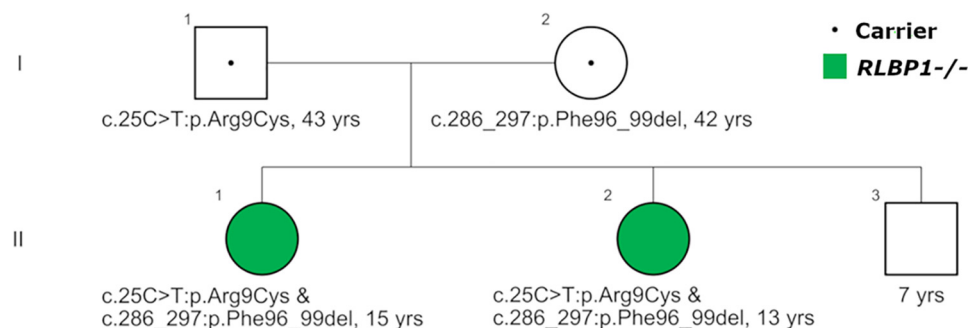


**Figure 1. Autosomal recessive inheritance patterns.** Affected female siblings (II-1; II-2; green filled circles) compound heterozygous for the missense mutation c.25C>T:p.Arg9Cys and c.286\_297:p.Phe96\_99 deletion in the *RLBP1* gene. Two generations (I, II) are shown. Male, square; female, circle. Retinitis punctata albescens patients, green filled symbol; carriers, dot in symbol; unknown, unfilled symbol.

mated that *RLBP1*-associated disease accounts for 0.5% of all RP cases (13), a condition that has a prevalence of 1 in 4000 in developed countries (14).

CRALBP in RPE cells participates in supplying 11-*cis*-retinal to both rods and cones, whereas cones also rely on 11-*cis* chromophore present in Muller cells (15–17). CRALBP performs multiple functions in the visual cycle. First, by noncovalently binding 11-*cis*-retinal as it is produced by the isomerase RPE65, CRALBP reduces product inhibition of the isomerase activity (18, 19) thereby ensuring efficient production of 11-*cis*-retinol. CRALBP can bind both 11-*cis*-retinol and 11-*cis*-retinal (16) thereby facilitating the oxidation of protein-bound 11-*cis*-retinol to 11-*cis*-retinal, catalyzed by retinol dehydrogenase 5 (RDH5) (16, 20). Accordingly, delayed dark adaptation is exhibited by human patients carrying a mutation of the *RLBP1*/*CRALBP* gene and by *Cralbp*<sup>-/-</sup> mice (1, 2, 9). Additionally, the hydrophobic pocket of CRALBP imposes a conformational strain on 11-*cis*-retinal and thus maintains the isomeric state of 11-*cis*-retinal even in the presence of light (21–24). As a retinaldehyde carrier CRALBP also protects against unwanted aldehyde toxicity (16).

Here we report findings in two siblings with early-onset retinal disorders who were compound heterozygous for two pathogenic mutations in the *RLBP1* gene. Previously unreported features of *RLBP1*/*CRALBP* disease in the affected patients are presented and replication in *Cralbp*<sup>-/-</sup> mice is demonstrated. Importantly, to the best of our knowledge, this is the first work to show a phenotype in asymptomatic human carriers of *RLBP1*/*CRALBP* mutations.

## Results

### *RLBP1*/*CRALBP*-associated disease in affected human patients

A family with two clinically affected female siblings (Fig. 1), a 15-year-old (II-1) and a 13-year-old (II-2), presented to the Department of Ophthalmology at Columbia University Irving Medical Center with a complaint of photophobia and poor night vision over the prior year. The younger brother (II-3) and the parents (I-1 and I-2) were asymptomatic. Whole exome sequencing of DNA obtained from peripheral blood revealed that both children were compound heterozygous for the missense mutation c.25C>T:p.Arg9Cys and c.286\_297:p.Phe96\_99 deletion in the *RLBP1* gene and diagnosis of RPA was made. These mutations have been reported

previously (11, 25). Concurrent genetic analyses of the parents revealed that the father is heterozygous for the c.25C>T:p.Arg9Cys mutation and the mother is heterozygous for the c.286\_297:p.Phe96\_99del variant (Fig. 1). Clinical and genetic characteristics of the patients and parents are summarized in Table 1.

### Full-field electroretinogram (ffERG)

ffERGs were performed in both scotopic and photopic states. Standard dark-adapted (30 min) rod-specific ERGs were extinguished in both daughters (II-1 and II-2; Fig. 2, top rows). Light-adapted 30-Hz flicker and single-flash were within the normal range (Fig. 2, middle rows). Interestingly, after prolonged dark-adaptation (>8 h overnight eye-patch), the rod responses measured by ERG increased to the normal range (Fig. 2, bottom rows). The young brother (II-3) had normal ERG results (not shown).

### Fundus imaging

In ultrawide-field (UWF) pseudo-color fundus images (200°), the patients exhibited radially arranged white spots that were more visible in peripheral retina (Fig. 3, A and B). The white spots were also more pronounced in the older sibling. UWF-autofluorescence/green (UWF-AF/green) images using 532 nm excitation provided images that were largely grainy but the optic disk and retinal vessels were visible (Fig. 3, C and D). The fovea was detected as a small dark zone with surrounding speckled brightness. The horizontally oriented oval-shaped central zone of increased brightness that in healthy eyes envelopes the macula and optic disk and is typical of UWF-AF/green fundus images (26) was less pronounced.

In both siblings, SW-AF (blue) images acquired with 488 nm excitation presented with typical central hypoautofluorescence but contrasting foveal darkness was not evident (Fig. 3, E and G). Outside the zone of reduced autofluorescence was a ring of speckled autofluorescence that at greater eccentricity transitioned into faintly autofluorescent macular spots and mottling.

Near-infrared autofluorescence (NIR-AF) fundus images obtained from both children presented with the central elevated intensity that is characteristic of healthy eyes and that is attributable to increased melanin optical density (Fig. 3, F and H). Hypoautofluorescent dots surrounded by areas of

**Table 1**  
Clinical and genetic characteristics of the family members

Patient	Gender	Age	Clinical symptoms	BCVA <sup>a</sup> (logMAR)		qAF8		Genetics
				OD	OS	OD	OS	
I-1	M	43	No symptoms	0.0	0.0	183	155	<i>RLBP1</i> <sup>+/-</sup> c.25C>T:p.Arg9Cys
I-2	F	42	No symptoms	0.0	0.0	114	118	<i>RLBP1</i> <sup>+/-</sup> c.286_297:p.Phe96_99del
II-1	F	15	Photophobia, poor night vision	0.06	0.06	–	–	<i>RLBP1</i> <sup>-/-</sup> c.25C>T:p.Arg9Cys and c.286_297:p.Phe96_99del
II-2	F	13	Photophobia, poor night vision	0.06	0.24	–	–	<i>RLBP1</i> <sup>-/-</sup> c.25C>T:p.Arg9Cys and c.286_297:p.Phe96_99del
II-3	M	7	No symptoms	0.02	0.02	N/A	N/A	NA <sup>b</sup>

<sup>a</sup> BCVA, best corrected visual acuity; logMAR, logarithm of the minimum angle of resolution; OD, right eye; OS, left eye; qAF8, average quantitative autofluorescence of the 8 segments of the ring at an eccentricity of approximately 7° to 9° from the fovea.

<sup>b</sup> NA, not applicable.

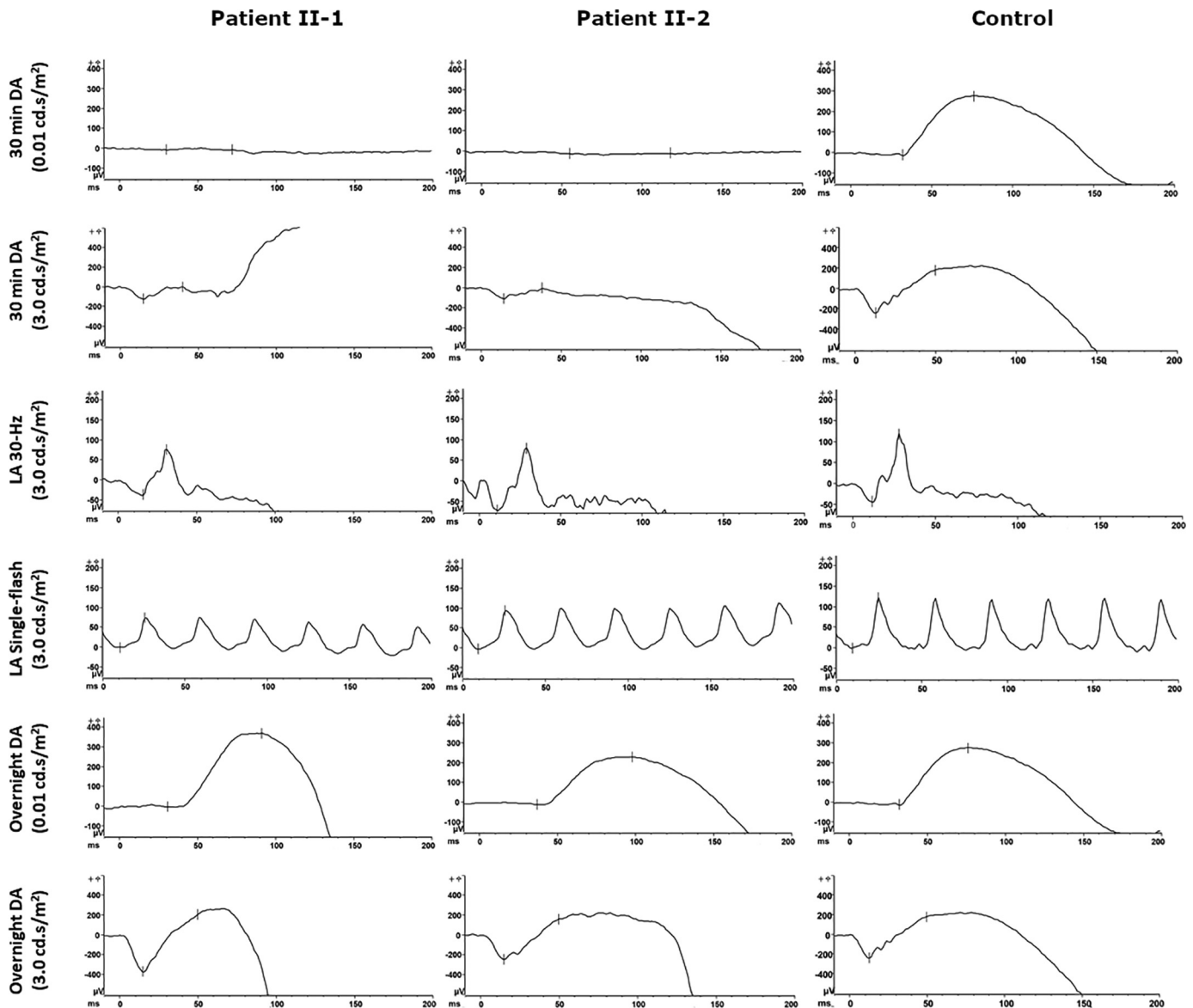
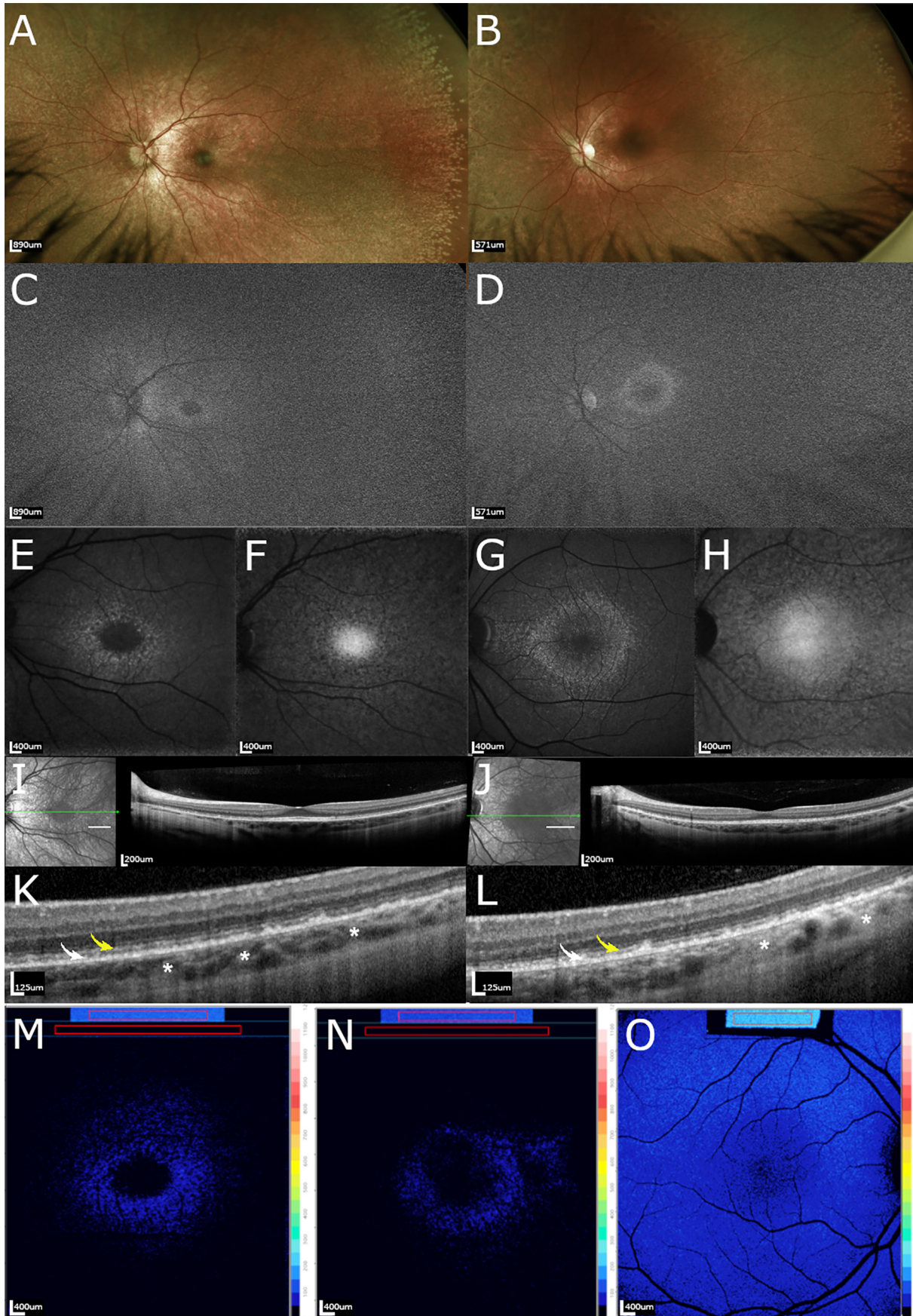


**Figure 2. Rod-cone dysfunction in fERG.** Patients II-1 and II-2: rod-specific ERG with 0.01 cd.s/m<sup>2</sup> stimulus following standard 30-min dark adaptation was absent. Maximum ERG (3.0 cd.s/m<sup>2</sup>) had a diminished response. Photopic ERG was within the normal range. After prolonged dark-adaptation (>8 h overnight eye-patch), rod-specific ERG and maximum ERG responses were recovered. Normal control is shown in the *right column*. DA, dark-adapted; LA, light-adapted.

apparently normal fluorescence were present in the parafoveal region.

In SD-OCT scans, hyperreflective aberrations were observed in II-1 and II-2 (Fig. 3, I and K, J and L). These changes were

characterized by undulations and discontinuities of the ellipsoid zone (*yellow arrows*), hyperreflective irregularities in the interdigitation zone (*white arrows*), and foci of hypertransmission into the choroid (*white asterisks*). These abnormalities



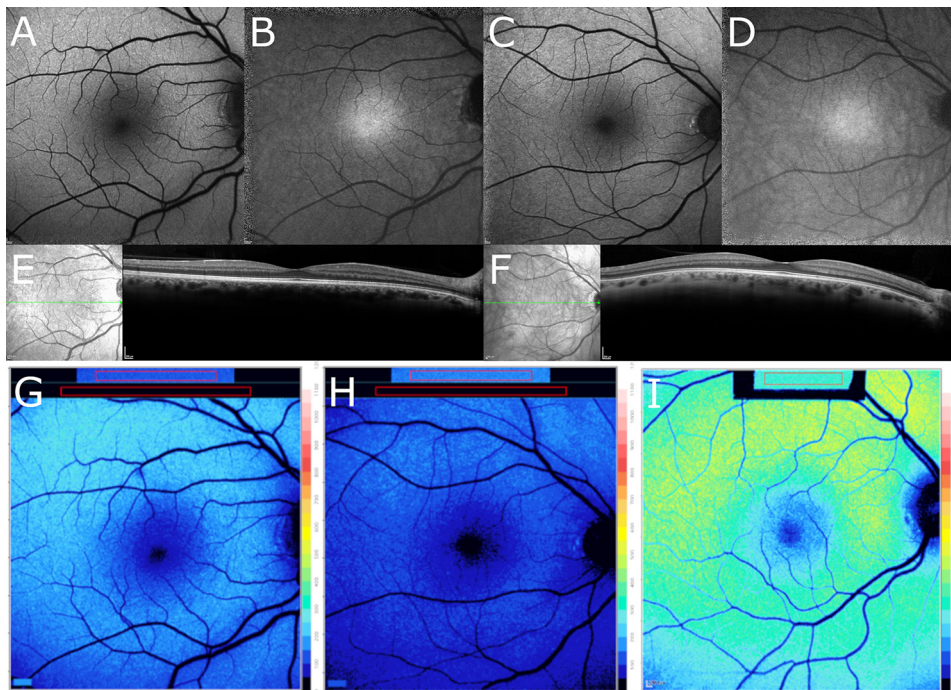


**Figure 4. Fundus images of the parents who are carriers of mutations in *RLBP1/CRALBP*.** Subjects I-1 (left) and I-2 (right). Subject I-1 is heterozygous for c.25C>T mutation in the *RLBP1* gene and subject I-2 is heterozygous for the c.286\_297del variant in the *RLBP1* gene. The C.289\_297:p.Phe96\_99 deletion carrier has less autofluorescence than the missense mutation c.25C>T:p.Arg9Cys carrier. A and C, SW-AF. Images acquired in normalized mode do not reveal differences in gray level intensities. B and D, NIR-AF. The fovea exhibits typical elevated intensity; contrast with AF in periphery appears to be increased. E and F, SD-OCT. Reflectivity layers appear normal. G–I, color-coded qAF images of the carriers I-1 (G), I-2 (H), and an age-matched healthy eye (I). Reduced qAF characterizes the symptomless carriers.

were observed in both siblings and were more pronounced in nonfoveal macula (Fig. 3, K and L). In both patients the external limiting membrane was continuous.

#### Quantitation of fundus images in affected patients and carrier parents

SW-AF originates from bisretinoid by-products of the visual cycle. To assess SW-AF intensities, the quantitative fundus autofluorescence (qAF) approach was used to measure intensities in the two patients and their parents. In the two *RLBP1/CRALBP*-affected siblings, qAF intensities within the concentric segments positioned at an eccentricity of 7–9° were not measurable. This profound and uniform reduction in qAF was evident in qAF color-coded images (Fig. 3, M and N) when comparison was made to a healthy control eye of similar age (Fig. 3O).

Importantly, although the carrier parents did not present with visual symptoms and SW-AF, NIR-AF and SD-OCT images were unremarkable (Fig. 4, A–F), in both parents color-coded qAF images revealed lower SW-AF intensities (Fig. 4, G and H) than in an age-similar healthy eye (Fig. 4I). The qAF value calculated as the mean of the 8 concentric segments was below the 95% confidence interval of healthy eyes (Fig. 5A). qAF was also lower in the mother who carried the c.286\_297:

p.Phe96\_99 deletion than in the father who was a heterozygous carrier of the c.25C>T:p.Arg9Cys mutation.

Melanin-derived NIR-AF (27–30) intensities originating primarily in RPE were measured along a horizontal axis through the fovea and were compared with the measurements obtained from a group of 19 healthy subjects that served as control. Interestingly, intensities in the NIR-AF profiles were decreased in both the probands and heterozygous parents (Fig. 5B); this reduction is indicative of RPE involvement in the disease processes. It is important to note that as with qAF, the reduction in the central NIR-AF signal was more pronounced in the carrier (mother) bearing the c.286\_297:p.Phe96\_99 deletion than in the carrier (father) harboring the missense mutation c.25C>T:p.Arg9Cys carrier. The affected siblings were compound heterozygous and exhibited a difference in the NIR-AF profiles. Although younger, the 13-year-old sibling presented with a greater decrease in NIR-AF. This finding deserves further investigation.

#### *Crabp*<sup>-/-</sup> mice: UPLC measurement of retinoids

CRALBP deficiency does not block the functioning of the visual cycle but is considered to modulate its kinetics (2). Thus to test the efficiency of CRALBP activity, we measured retinoid

**Figure 3. Multimodal images in siblings deficient in CRALBP.** Images of II-1 (left) and II-2 (right) both of whom are compound heterozygous for mutations in the *RLBP1* gene. A and B, UWF color fundus photographs. Note the radially arranged white dots more visible in the peripheral retina. C and D, green UWF autofluorescence. Fovea was detected as a small dark zone with surrounding speckled brightness. E and G, SW-AF. A ring of speckled hyperautofluorescence transitioned into faintly autofluorescent macular spots and mottling at greater eccentricity. F and H, NIR-AF. The fovea exhibits the characteristic elevated NIR-AF intensity. Hypoautofluorescent dots surrounded by areas of normal fluorescence in the parafoveal region can be appreciated. I, J, and K, L, SD-OCT. Note undulations of the ellipsoid zone (yellow arrows), hyperreflective irregularities in the interdigitation zone (white arrows), and foci of hypertransmission into the choroid (white asterisks). K and L represent magnified images of the area indicated by the short white lines in I and J. M–O, color coded quantitative fundus autofluorescence images. Patients II-1 (M) and II-2 (N) had undetectable levels of AF except for a parafoveal ring. A healthy control eye 11-year-old subject is shown (O).

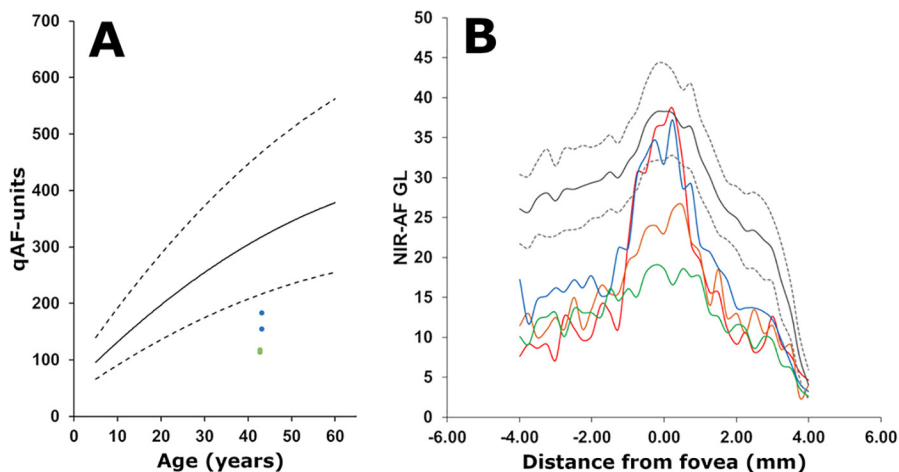


**Figure 5. Quantitation of fundus autofluorescence.** *A*, short-wavelength (488 nm) fundus autofluorescence measured as qAF at an eccentricity of 7–9° and plotted as a function of age. Mean qAF<sub>8</sub> of parents (blue, l-1; and green l-2) are plotted together with mean (solid black line) and 95% confidence levels (dashed lines) acquired from eyes of healthy subjects. Note that qAF intensities at the same location in the affected siblings were not measurable. *B*, semi-quantitative NIR-AF intensity profiles plotted as a function of temporal-to-nasal (left to right) distance (mm) along a horizontal line through the fovea (0). Gray lines represent mean (solid lines) and 95% confidence intervals (dashed lines) of healthy control eyes. Subjects are represented as follows: blue line, l-1; green line, l-2; red line, ll-1; orange line, ll-2.

levels in dark-adapted mice (Fig. 6, *A* and *B*). To enable extraction efficiency the nucleophile hydroxylamine was used to promote 11-*cis*-retinal release from the stable retinal oxime derivatives (anti and syn) ( $\lambda_{\max}$ , 367 nm) (31). Measurements of 11-*cis*-retinal in 2-month-old dark-adapted WT mice were similar to values previously reported (32, 33). Meanwhile in *Cralbp*<sup>-/-</sup> mice, 11-*cis*-retinal measured as picomoles per eye was significantly lower than in WT mice ( $p < 0.001$ , ANOVA and Sidak's multiple comparison test were used) (Fig. 6*C*). However, expressed as a fraction of total retinoid there was no significant difference (Fig. 6*D*), as was previously reported (1). Amounts of 11-*cis*-retinol were also lower in the *Cralbp*<sup>-/-</sup> mice (Fig. 6*E*).

We also monitored the recovery of retinoid levels following visual pigment bleaching (white light, 8200–900 lux, 3 min) in dark-adapted *Rlbp1/Cralbp*<sup>-/-</sup> and WT mice. With 1 and 2 h in the dark after photobleaching, there was no evidence of recovery of 11-*cis*-retinal levels in the *Rlbp1/Cralbp*<sup>-/-</sup> mice and 11-*cis*-retinal was significantly lower than in WT mice (Fig. 6*F*). Conversely, all-*trans*-retinyl ester amounts were significantly higher at 1 and 2 h after the photobleach (Fig. 6*G*). As a percent of dark-adapted pre-bleach levels, all-*trans*-retinal was higher immediately after photobleaching (data not shown).

#### Fundus imaging in mice

In the *Cralbp*<sup>-/-</sup> and WT mice, we imaged *in vivo* fundus autofluorescence using instrumentation similar to that employed clinically. SW-AF (488 nm) images were uniformly low in intensity and due to poor contrast blood vessels were muted (Fig. 7*A*). The brightness of the internal fluorescent reference in the qAF images (488 nm) attested to the long exposure time used to generate the fundus AF in these mice. Puncta were not observed in the fundus.

Measurement of SW-AF by qAF revealed that fundus intensities were significantly lower in the *Cralbp*<sup>-/-</sup> mice as compared with the agouti 129S1/SvImJ mice from age 6 to 18 months (Fig. 7*B*). qAF in the *Cralbp*<sup>-/-</sup> mice also declined at 9 months of age and was significantly lower at 18 months ( $p < 0.05$ ).

NIR-AF intensities in *Cralbp*<sup>-/-</sup> mice at 6 and 9 months of age were similar to that of agouti WT at ages 2, 6, and 9 months (Fig. 7*C*). Levels then dropped significantly at 12 and 18 months of age. In *Cralbp*<sup>-/-</sup> mice NIR-AF intensities at 12 and 18 months were significantly lower than in WT (Fig. 7*C*).

#### High performance LC (HPLC)

Because SW-AF was reduced in the *Cralbp*<sup>-/-</sup> mice we also measured the bisretinoid lipofuscin fluorophores that form as a by-product of the visual cycle and that serve as the source of this SW-AF emission. A representative HPLC chromatogram in Fig. 8 illustrates the detection of bisretinoids in an agouti WT mouse (2 eyes/sample). With identification using UV-visible absorbance spectra (monitoring at 430 nm) and retention times determined from authentic compound, elution peaks were assigned to the bisretinoids A2E ( $\lambda_{\max} = 431, 332$ ), iso-A2E ( $\lambda_{\max} = 426, 339$ ), A2GPE (A2-glycerophosphoethanolamine) ( $\lambda_{\max} = 448, 351$ ), and A2-DHP-PE (A2-dihydropyridinephosphatidylethanolamine) ( $\lambda_{\max} = 487, 335$ ) (Fig. 8*A*). Conversely, even in an extract from 10 eyes pooled from *Cralbp*<sup>-/-</sup> mice, A2E and iso-A2E were consistently less abundant than in a sample of 2 eyes from WT mice (Fig. 8*A*).

Because ultra-performance LC (UPLC) provides excellent sensitivity and resolution with smaller sample sizes than HPLC, we used UPLC for further quantitative analysis. A2GPE increased with age in both the *Cralbp*<sup>-/-</sup> and WT mice (Fig. 8*B*), but at all ages A2GPE was also significantly lower in *Cralbp*<sup>-/-</sup> than WT.

RPE65 is the isomerohydrolase responsible for converting all-*trans*-retinyl-ester to 11-*cis*-retinol within RPE cells (34–36) and *RLBP1/CRALBP*-associated disease is considered to share clinical features with *RPE65*-related dystrophy (37, 38). *Rpe65* null mutant (*Rpe65*<sup>-/-</sup>) mice do not generate 11-*cis*-retinal chromophore (39). A comparison of 6-month-old *Cralbp*<sup>-/-</sup> and *Rpe65*<sup>-/-</sup> mice (Fig. 8*C*) revealed that whereas A2GPE was reduced in *Cralbp*<sup>-/-</sup> mice, an A2GPE peak was undetectable in the *Rpe65*<sup>-/-</sup> mice even in a sample of 10 eyes.

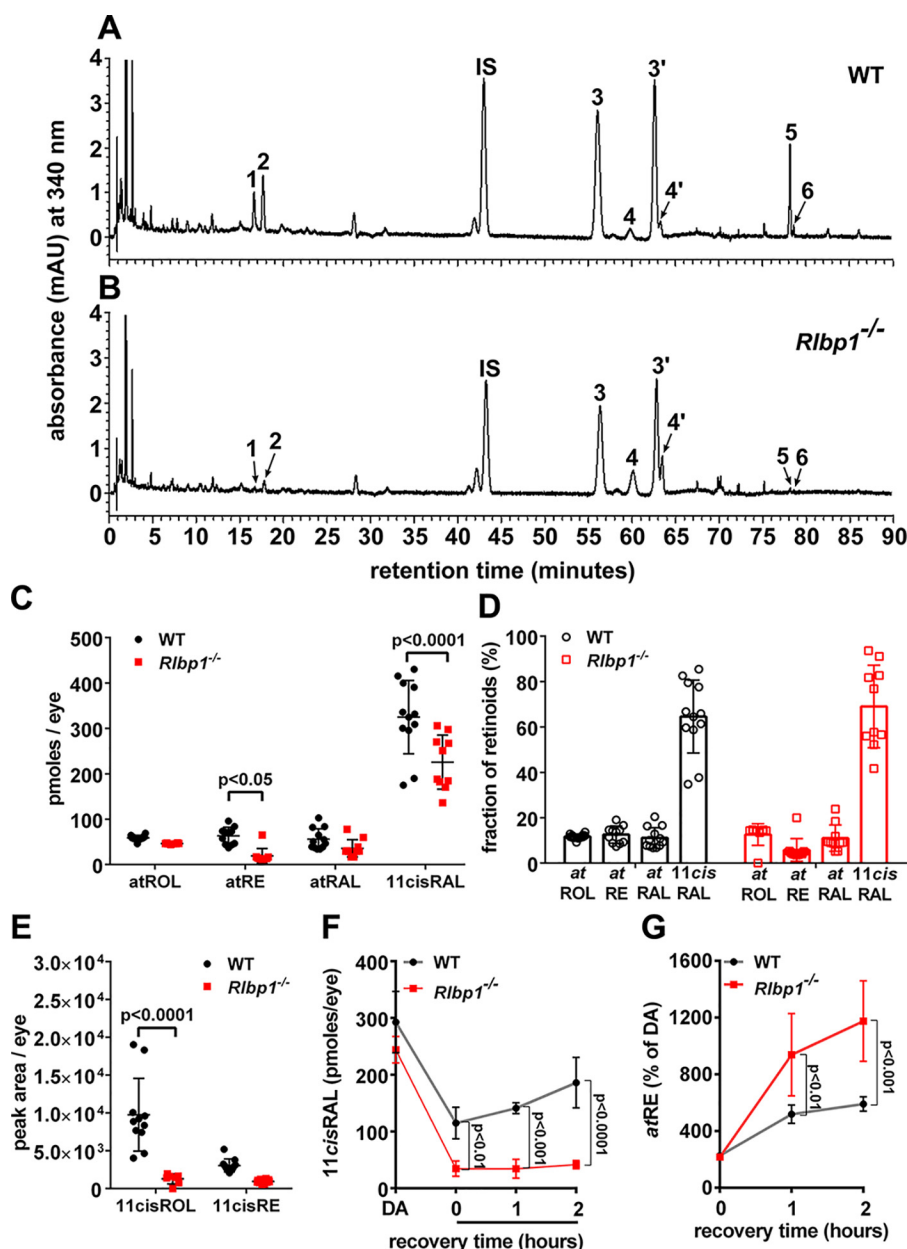


**Figure 6. Retinoid levels in dark-adapted agouti *Cralbp*<sup>-/-</sup> and WT mice.** Ages were 2–4 months. *A* and *B*, representative UPLC chromatograms demonstrating separation of hexane-extracted retinoids in eyes of agouti WT (*A*) and *Cralbp*<sup>-/-</sup> mice (*B*). Monitoring was done at 340 nm. Age 4 months; 1 eye/sample. The numbers indicate the identity of peaks based on comparison with standards. 1, 11-*cis*-retinol; 2, all-*trans*-retinol; IS, internal standard, all-*trans*-retinyl acetate; 3, anti 11-*cis*-retinal-(*O*-ethyl) oxime; 4, anti all-*trans*-retinal-(*O*-ethyl) oxime; 3', syn 11-*cis*-retinal-(*O*-ethyl) oxime; 4', syn all-*trans*-retinal-(*O*-ethyl) oxime; 5, all-*trans*-retinyl palmitate; 6, 11-*cis*-retinyl palmitate. *C* and *D*, quantitation of retinoids as picomoles/eye (*C*). Presentation of data in *C* as percentage of total retinoid (*D*). All-*trans*-retinol (*atROL*), all-*trans*-retinyl palmitate (*atRE*), all-*trans*-retinal (*atRAL*), 11-*cis*-retinal (11*cisRAL*) are shown. *E*, quantitation of 11-*cis*-retinol (11*cisROL*) and 11-*cis*-retinyl palmitate (11*cisRE*) as peak area/eye. *F* and *G*, levels of 11-*cis*-retinal (*F*) and all-*trans*-retinyl ester (*G*) in dark-adapted (*DA*) mice recovering from a photobleach for 1 and 2 h in the dark. Mean  $\pm$  S.D., 10–12 samples (*C*–*E*); 4 samples (*F* and *G*); *p* values determined by ANOVA and Sidak's multiple comparisons test.

### Analysis of outer nuclear layer (ONL) in *Cralbp*<sup>-/-</sup> mice

Because retinoids are also required to sustain the viability of photoreceptor cells (1, 16) we examined photoreceptor cell numbers by counting nuclei in the ONL (Fig. 9). The numbers of photoreceptor cell nuclei spanning the width of the outer nuclear layer in the WT mice at the age of 8–9 months was 10.0 ( $\pm$  0.38, S.D.) (Fig. 9A); this value was typical of the 9–11 range reported in the literature (40–47). In the *Cralbp*<sup>-/-</sup> mice at 8–9 months of age the mean number of nuclei was reduced to 8.6 ( $\pm$  0.48, S.D.) and at age 12 months a further reduction to

7.32 ( $\pm$  0.44, S.D.) (*p* < 0.05; two-way ANOVA and Sidak's multiple comparisons test) occurred (Fig. 9, *A* and *B*).

### Discussion

We have presented the clinical and molecular analyses of two siblings compound heterozygous for disease-causing mutations in the *RLBP1* gene, their carrier parents, and *Cralbp*<sup>-/-</sup> mice. By employing multiple imaging modalities, we observed that the dot-like puncta characteristic of color fundus images in *RLBP1*-disease (11, 12) were prominent and radially arranged

## RLBP1/CRALBP gene deficiency

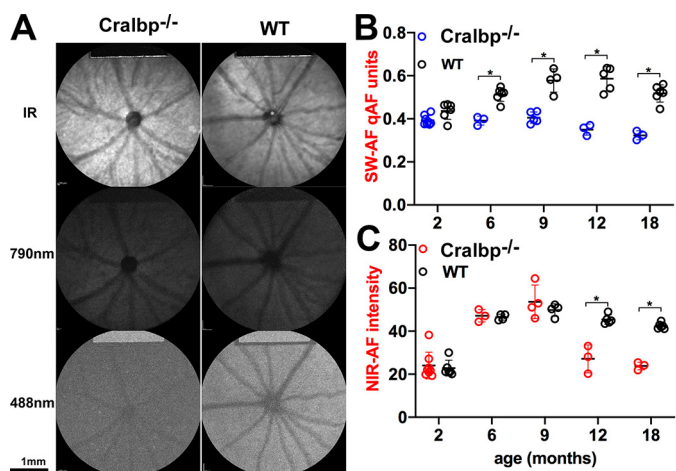


**Figure 7. Fundus images acquired from agouti *Cralbp*<sup>-/-</sup> and WT mice.** A, IR reflectance (IR; 820 nm), SW-AF (488 nm), and NIR-AF (790 nm) images acquired from agouti *Cralbp*<sup>-/-</sup> and WT mice (age 6 months). B, SW-AF intensities were measured in agouti *Cralbp*<sup>-/-</sup> and WT mice with qAF protocols and plotted as a function of age. Gray levels were measured 8.25–19.25° from the disc center and were normalized to gray levels in an internal fluorescent reference (rectangular area at top of image) to calculate qAF. Means of 3–8 mice; \*,  $p < 0.05$ , ANOVA and Sidak's multiple comparisons test. C, NIR-AF intensities were measured in agouti *Cralbp*<sup>-/-</sup> and WT mice. Mean  $\pm$  S.D. of 3–8 mice; \*,  $p < 0.05$ , ANOVA and Sidak's multiple comparisons test.

in peripheral retina when viewed by UWF imaging. These puncta were also autofluorescent in SW-AF images and hypofluorescent in NIR-AF images. The SD-OCT scans presented foci of abnormal outer retinal reflectivity together with hypertransmission of SD-OCT signal into the choroid. Full-field ERG recordings revealed that rod responses in the affected siblings were severely depressed. Nevertheless, to our knowledge this is the first report to show that after prolonged dark-adaptation the patients with RPA recovered their rod-specific ERG responses. This finding together with reduced levels of 11-*cis*-retinal and 11-*cis*-retinol in the *Cralbp*<sup>-/-</sup> mice confirmed that a deficiency in CRALBP does not block the enzymatic production of 11-*cis*-retinoid but 11-*cis*-retinal is regenerated at a slower rate. The reduction in SW-AF intensity measured as qAF in the affected adolescents, the two carriers and *Cralbp*<sup>-/-</sup> mice are corroborated by HPLC quantitation of bisretinoids in the mice and results from reduced availability of visual chromophore.

We gained insight into the structural correlates of the white spots. The hypopigmentation evinced as white dots in pseudocolor fundus images and as reduced melanin signal (27–30) in NIR-AF images indicated a change in the RPE monolayer, whereas hypertransmission of the SD-OCT signal posterior to the RPE was indicative of RPE atrophy at these positions. We have previously observed that outside the macula of *GPR143/OAI* carriers, pigmented and nonpigmented RPE cells segregate into radial arrays (29) not unlike the pattern of radially arranged dots observed in the UWF pseudocolor images (Fig. 3, A and B) of the current study. This similarity suggests that the pattern of dot-like lesions is established by RPE cells. Perhaps the reduction in melanin signal recorded by NIR-AF (27–30) reflects a remodeling of the RPE monolayer to fill gaps left by RPE loss. The involvement of RPE in the atrophy associated with *RLBP1/CRALBP* disease is indicated in other studies by

the hyperfluorescence observed in fluorescein angiograms (9) and by the same hypertransmission of SD-OCT signal into the choroid at sites of atrophy (10). It has also been noted that the dot-like fundus lesions progress to RPE atrophy (6). Here the reduced melanin-derived NIR-AF signal was not restricted to the *RLBP1/CRALBP*-affected and *Cralbp*<sup>-/-</sup> mice, instead this phenotype was also exhibited by the heterozygous carrier parents.

In the SD-OCT scans presented here the abnormal foci of hyperreflectivity in photoreceptor-attributable bands was limited to the IZ and EZ bands perhaps because of the younger ages of the affected siblings. In previous reports, however, these focal lesions incorporated EZ, external limiting membrane, and extended into the ONL (48) thus replacing photoreceptor cell-attributable bands. The degenerative changes in photoreceptor cells indicated by these SD-OCT findings are corroborated by the reduced ONL area in *Cralbp*<sup>-/-</sup> mice.

The reduction in qAF in *RLBP1/CRALBP*-affected patients and *Cralbp*<sup>-/-</sup> mice and in HPLC quantified bisretinoid in *Cralbp*<sup>-/-</sup> mice is attributable to chronic deficiency in the 11-*cis*-retinal chromophore. Indeed we observed attenuated qAF even in the asymptomatic carrier parents carrying a single mutant allele. This finding indicates that a reduction of approximately half of the gene product reduces bisretinoid. Because bisretinoid lipofuscin accumulation underlies retinal diseases such as recessive Stargardt disease, various strategies aimed at reducing bisretinoid formation have been investigated in recent years (49–59). Here we show for the first time that slowing the visual cycle by a deficiency in CRALBP activity associated with biallelic mutations (patients) or even a mutation in one allele (parent carriers) also confers a decrease in bisretinoid lipofuscin. Moreover, our findings suggest that quantitation of autofluorescence may be used as a predictor of mutation severity as it showed a difference between the missense and deletion variants in the carriers.

Several findings in *Cralbp*<sup>-/-</sup> mice replicated the disease features observed in the *RLBP1/CRALBP*-affected patients. Consistent with the abnormal ERG responses in the patients, 11-*cis*-retinal was significantly lower in *Cralbp*<sup>-/-</sup> mice than in the WT. Measurement of SW-AF by qAF showed that fundus intensities were significantly lower in the *Cralbp*<sup>-/-</sup> mice in keeping with the reduced qAF recorded in the patients. Moreover, HPLC quantitation of the bisretinoid visual cycle by-products, the source of SW-AF, was also reduced in the mutant mice. NIR-AF intensities originating primarily in RPE cells were found to be reduced in mice at 12 and 18 months of age and correspondingly, were reduced in the affected patients. Consistent with the central atrophy observed in RPA (10, 11) and with the SD-OCT evidence of structural aberration in photoreceptor cells observed here, we found that the numbers of photoreceptor cell nuclei spanning the width of ONL was decreased by 30% at age 12 months in *Cralbp*<sup>-/-</sup> versus WT mice.

The CRALBP Phe96–99del mutation results in the loss of four residues, three of which are hydrophobic (Phe-96, Leu-97, and Phe-99) and one is charged (Arg-98); all are located on helix  $\alpha 4$  of the N-terminal all-helical  $\alpha$  domain. Although this region is  $\sim 25$  Å away from the ligand-binding pocket of CRALBP,

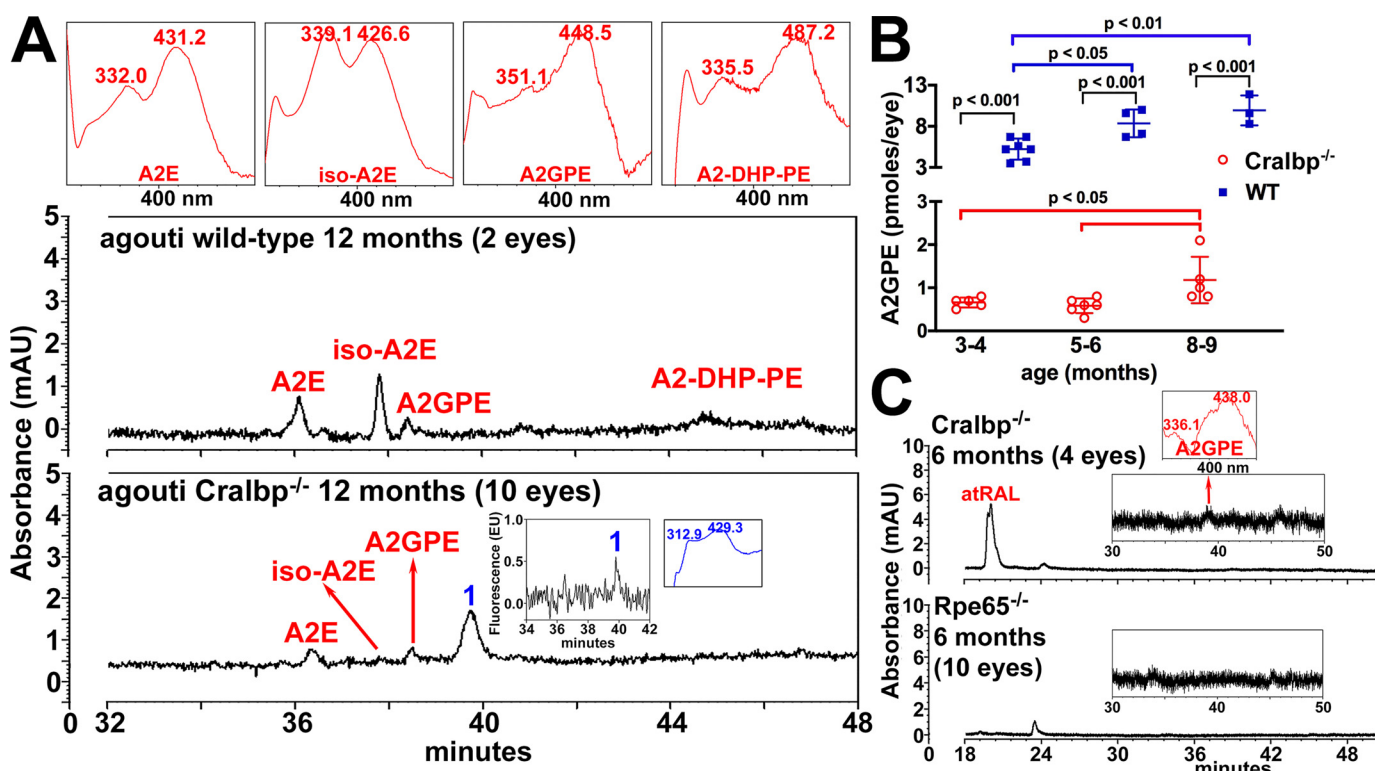


**Figure 8. Reduced bisretinoids in *Cralbp*<sup>-/-</sup> mice retinæ.** HPLC analysis of bisretinoids in WT and *Cralbp*<sup>-/-</sup> mice. **A**, representative reverse phase HPLC chromatograms with monitoring at 430 nm, illustrate the detection of the bisretinoids identified on the basis of UV-visible absorbance and retention times (*R<sub>t</sub>*) recorded using authentic standards. A2E (*R<sub>t</sub>* 36.5 min), iso-A2E (*R<sub>t</sub>* 37.8 min), A2GPE (*R<sub>t</sub>* 38.4 min), A2-DHP-PE (*R<sub>t</sub>* 45.1 min) and oxidized bisretinoid (1, *R<sub>t</sub>* 39.7 min). Age was 12 months. *Insets*: top, UV-visible absorbance spectra of chromatographic peaks corresponding to bisretinoids, *inset*, fluorescence at  $\lambda_{ex} = 430$  nm/ $\lambda_{em} = 600$  nm and UV-visible absorbance of peak 1. **B**, quantification of bisretinoid in *Cralbp*<sup>-/-</sup> and WT mice. **C**, A2GPE is not detectable in *Rpe65*<sup>-/-</sup> mouse eyecups analyzed by UPLC. Eyecups from pigmented *Cralbp*<sup>-/-</sup> and WT mice were analyzed by UPLC with a BEH phenyl column and monitoring at 430 nm. Values are mean  $\pm$  S.D. of 3–7 independent samples. 2–4 eyes/sample. *p* values were determined by one-way ANOVA and Tukey’s multiple comparison tests.

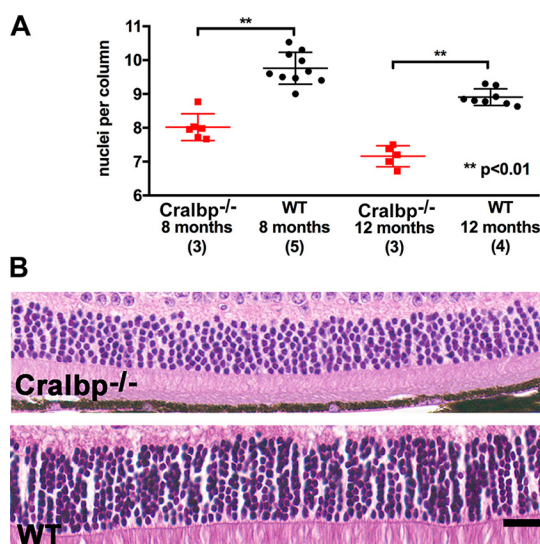


**Figure 9. Photoreceptor cell loss in *Cralbp*<sup>-/-</sup> mice.** **A**, numbers of nuclei per column extending the width of the ONL. Mean  $\pm$  S.D.; *Cralbp*<sup>-/-</sup>, 6 eyes (age 8–9 months), 5 eyes (age 12 months); WT: 10 eyes (age 8–9 months); 8 eyes (12 months). **B**, representative light micrographs of inferior hemiretina of *Cralbp*<sup>-/-</sup> and WT mice (age 12 months) within 500–1000  $\mu$ m from the optic nerve head.

insights into potential structure-function relationship can be gained from the R234W mutant crystal structure (23). The conformation of Arg-234 is essential for normal activity of CRALBP. Disruption of the Arg-234 conformation in the

R234W mutant crystal structure resulted in a cascade of side chain conformational changes that ultimately affected the 11-*cis*-retinal-binding site and resulted in a 5-fold decrease in enzymatic activity.

The long-range effects of this single mutation at position Arg-234 (Fig. 10, blue residue) and the resulting structural rearrangements of three hydrophobic residues (Fig. 10, light pink) underscore the importance of this region for maintaining normal protein function. Deletion of residues 96–99 could alter the conformation of Arg-234 by preventing its interaction with Glu-51, with which it makes direct contact in the native crystal structure (C–O to *n* = O distance = 2.7 Å); this would also affect the retinal-binding pocket. Furthermore, Phe-99 interacts with Pro-232 (Fig. 10, black) and loss of Phe-99 could alter the conformation of the nearby Arg-234 by disruption of this interaction. These potential structural rearrangements within the Phe96–99del mutant provide a theoretical basis for decreased enzymatic activity through long-range disruption of the 11-*cis*-retinal-binding site, similar to that seen in the R234W crystal structure.

It is also possible that loss of the three hydrophobic residues Phe-96, Leu-97, and Phe-99, and the charged Arg-98 in the Phe96–99del mutation disrupt the structure and function through a different, unknown mechanism. For example, the absence of these residues could perturb nearby residues that make contacts critical for stabilizing the retinal-binding site or

## RLBP1/CRALBP gene deficiency

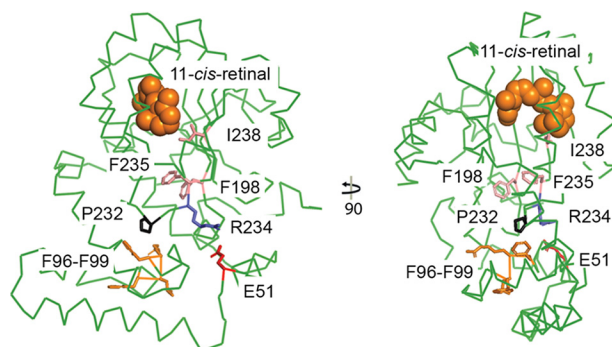


**Figure 10. Crystal structure of CRALBP.** Two views of the CRALBP crystal structure (PDB 3HY5) with key residues colored as indicated. Residues in *light pink* (I198, F235, and I238) underwent conformational change in the R234W mutant crystal structure (PDB 3HX3, not shown) to alter 11-*cis*-retinal binding affinity and decreased enzymatic activity. Residues lost in the Phe96–99del mutant are shown in *orange* (F96, L97, R98, and F99) and the interacting Pro-232 is shown in *black*. 11-*cis*-retinal is depicted by *orange spheres*.

catalytic residues. Position 9 is in the disordered N terminus region of the crystal structure, so no structure–function relationship can be assessed for this region. Nevertheless, the R9C mutation could affect the pH dependence of enzymatic activity and this Arg-9 may be important in other conformational states.

What is the mechanism by which CRALBP deficiency causes RPE cell atrophy? The protein CRALBP in RPE cells serves as both an acceptor of 11-*cis*-retinol in the isomerization step of the visual cycle and as a facilitator of the oxidation of 11-*cis*-retinol to 11-*cis*-retinaldehyde (16, 60, 61). By chaperoning 11-*cis*-retinal it also protects against damage from free aldehyde. Whether the loss of the retinaldehyde-carrier function of CRALBP in the presence of regenerated 11-*cis*-retinal is permissive for unwanted aldehyde toxicity, remains to be determined in our ongoing studies.

The current qAF findings are of additional interest. It was noted previously that *Cralbp*<sup>−/−</sup> mice are protected from light damage (1) and it was suggested that *Cralbp* deficiency reduces the quantity of the mediator of light-mediated retinopathy (1). Based on age and genotype associations we have previously presented evidence implicating bisretinoids as the initiators of light damage (62). The reductions in bisretinoid and retinoid reported here likely reveal the mechanism by which *RLBP1/CRALBP* deficiency protects against light damage.

For the most part, treatments for arRP are not available. However, gene therapy currently exists for patients carrying *RPE65* mutations (63–65) that share some clinical features with *RLBP1/CRALBP* disease. Moreover, subretinal injection of an adeno-associated vector driving the expression of human CRALBP in *Cralbp*<sup>−/−</sup> mice improved both cone and rod electroretinographic responses (66, 67).

In summary, with deficiency in CRALBP, the cone and rod visual cycles fail to provide normal levels of visual chromophore. The latter deficiency manifests in *RLBP1/CRALBP*-affected patients as nonrecordable rod ERG responses that recover after prolonged dark adaptation. The chronically diminished 11-*cis*-retinal is realized as pronounced declines in bisretinoid visual cycle by-products, the source of SW-AF, in *RLBP1/CRALBP*-affected patients, and with lesser declines

in symptomless *RLBP1/CRALBP* carriers. The reductions in qAF and NIR-AF intensities in the affected patients and in their heterozygous parents have not previously been reported. Indeed these decreases in qAF and NIR-AF are indicative of RPE changes in heterozygous carriers and signify a phenotype not previously recognized in humans heterozygous for *RLBP1/CRALBP* mutations.

## Experimental procedures

### Human patients

The patients presented to the Department of Ophthalmology, Columbia University Medical Center. Each patient had a complete ophthalmic examination that included best-corrected visual acuity, tonometry and anterior segment, media and fundus examination. Pupils were dilated with topical 1% tropicamide and 2.5% phenylephrine before imaging and fundus examination. The patients provided written informed consent under a protocol approved by the Institutional Review Board of Columbia University. The study was approved by the Institutional Review Board at Columbia University and adhered to tenets established by the Declaration of Helsinki.

### Electroretinography

ffERG were performed in the patients according to the standards from the International Society for Clinical Electrophysiology (ISCEV) using the Diagnosys Espion Electrophysiology system (Diagnosys LLC, Lowell, MA) and Dawson Trick Litzkow (DTL) fiber electrodes in both scotopic and photopic states.

### Fundus imaging

Horizontal SD-OCT scans (9 × 9 mm scans; 870 nm; 7 μm axial resolution) through the macula were acquired by cSLO (confocal scanning laser ophthalmoscopy; Spectralis HRA+OCT, Heidelberg Engineering, Heidelberg, Germany) in high-resolution mode with an average of 100 single scans. The scans were registered automatically to a simultaneously acquired IR reflectance (IR-R) (820 nm) fundus image. Nomenclatures used to identify reflectivity bands in SD-OCT images were as published (68).

SW-AF images (488 nm excitation; emission 500 to 680 nm; 30° × 30° field) were obtained using a cSLO (Spectralis) HRA+OCT (Heidelberg Engineering, Heidelberg, Germany). For qAF, images were acquired and analyzed as described previously (69–72) using a Spectralis HRA+OCT equipped with an internal fluorescent reference for correction of variable laser power and differences in detector sensitivity. The images were acquired in high-speed mode (8.9 frames/s), as a minimum of 12 frames (video format) and saved in nonnormalized mode. A minimum of 6 frames per video was required for the analysis. Two sessions of three videos each were performed per eye. An averaged nonnormalized image was generated from each video and the two best images from each session were analyzed (4 averaged images per eye).

Mean gray levels were determined in eight circular segments, positioned 7 to 9° from the fovea. Vessels in the sampling area, which would decrease the qAF level, were accounted for by the

software algorithm. qAF values were calculated after gray levels were calibrated to gray levels in the reference; and after accounting for the zero-gray level of the laser, refractive error, image magnification, and age-adjusted lens transmission (73). For each eye, a qAF value was computed as the mean of the qAF values of the segments (qAF<sub>s</sub>). The healthy control group (74) was composed of 87 subjects of white ethnic background with an age range of 5 to 58 years old. Color-coded qAF maps were computed based on pixel-wise transformation of qAF values (WaveMetrics, Lake Oswego, OR).

NIR-AF (790 nm excitation, >830 nm emission, 30 × 30° field) images were obtained with a Heidelberg Retina Angiograph 2 scanning laser ophthalmoscope (HRA2-cSLO, Heidelberg Engineering, Heidelberg, Germany) using the indocyanine-green angiography mode. To obtain high-quality images, the eye-tracking function was utilized, and 100 single frames were averaged and saved in normalized mode. Semi-quantitative analysis of NIR-AF imaging was also performed. With a sensitivity of 96 (within a range of 51–100%) and the eye-tracking function, 100 single frames were averaged to obtain high-quality images saved in nonnormalized mode. ImageJ (RRID: SRC\_003070; provided in the public domain by the National Institutes of Health, Bethesda, MD) was used to analyze and plot the NIR-AF signal. Nineteen subjects (mean age 35.96 years) without a history of eye disease served as the healthy-eye group. These individuals self-identified as Caucasian (11), African American (3), Asian (3), and Hispanic (2).

UWF pseudocolor images were acquired using the Optos 200 Tx imaging system (Optomap Daytona, United Kingdom, Scotland; lasers: red, 633 nm; and green, 532 nm) with red and green false-color display. UWF-AF/green were also acquired (532 nm excitation; 570–780 emission; 200° field).

For analysis, all images were registered and aligned using i2k Retina software (Dual Align LLC, Clifton Park, NY). For illustrative purposes, some nonaligned images were used in figures.

## Mice

Cralbp<sup>-/-</sup> mice (Rpe65–Leu-450; agouti) were obtained as a gift from Dr. Vladimir J. Kefalov, and were bred in-house. 129S1/SvImJ mice (Rpe65–Leu-450; agouti) and Rpe65<sup>-/-</sup> mice (Rpe65<sup>Rd12</sup>; black) were purchased from The Jackson Laboratories, Bar Harbor, ME. Animal protocols were approved by the Institutional Animal Care and Use Committee of Columbia University and complied with guidelines set forth by the ARVO Animal Statement for the Use of Animals in Ophthalmic and Vision Research. Mice were free of the Crb1/Rd8 mutation.

## Analysis of retinoid in mice eyes

For UPLC quantitation of retinoids, frozen mouse eyecups (1 eye/sample) were homogenized and derivatized with *O*-ethylhydroxylamine (100 mM; 1 ml, on ice) in Dulbecco's phosphate-buffered saline (pH 6.5, without CaCl<sub>2</sub> and MgCl<sub>2</sub>) using glass homogenizers. After vortexing, samples were allowed to stand for 15 min at 4 °C. All-*trans*-retinyl acetate was added to each sample as an internal standard. Methanol (1 ml) was added and the samples were vortexed and extracted with hexane (3 ml, 3 times). After centrifugation (1500 × *g* for 5 min at 4 °C), the hexane phase was dried under argon gas and then resuspended

in 20 μl of acetonitrile. For separation, a Waters Acquity UPLC-PDA system (Waters, Milford, MA) was used with a CSH C18 column (1.7 μm, 2.1 × 100 mm) and gradients of water (A) and acetonitrile (B) with 0.1% of formic acid as follows: starting at 60% B; holding for 5 min; a linear increase to 70% B over 55 min; a linear increase to 100% B over 10 min; holding for 20 min. The flow rate was 0.3–0.5 ml/min. RAL (*O*-ethyl) oximes were monitored at 360 nm and all-*trans*-retinol and all-*trans*-retinyl palmitate were monitored at 320 nm. UV absorbance peaks were identified by comparison with external standards of synthesized 11-*cis*-retinal (*O*-ethyl) oxime, all-*trans*-retinal (*O*-ethyl) oxime, all-*trans*-retinol, and all-*trans*-retinyl palmitate. Molar quantities per eye were calculated based on standard solutions with concentrations determined spectrophotometrically. Peak areas were calculated using Waters Empower Software and results were analyzed in Excel (Microsoft, Redmond WA).

## qAF in mice

Mice were anesthetized, pupils were dilated, the cornea was lubricated, and mice were positioned as previously described (75–77). SW-AF images (488 nm, 55° wide-field lens; 0.98 mm detection pupil) were captured with a cSLO (Spectralis HRA; Heidelberg Engineering, Heidelberg, Germany) with laser power set at ~280 microwatts and sensitivity at 100–105, after visual pigment was bleached for 20 s. Nine successive frames were acquired in SW-AF high-speed mode and were saved as nonnormalized images. Mean gray levels (GL) in the SW-AF images were measured in 8 predefined segments and qAF at 488 nm excitation was calculated by normalization to the GL of the reference after subtraction of zero light (GL<sub>0</sub>) and inclusion of a reference calibration factor.

A mean of 100 frames were also obtained at 790 nm excitation (NIR-AF) with high resolution ART mode (Automatic Real-Time) and resized with Photoshop CS4 (Adobe Systems, San Jose, CA) to 768 × 768 pixels (equivalent to high-speed mode). Intensity at 790 nm was calculated by subtracting the minimal GL of optic nerve head measured by ImageJ (a public domain, Java-based image processing program developed at the National Institutes of Health).

## Measurement ONL

Mouse eyes were marked superiorly with tattoo ink (Ketchum Manufacturing Inc., Ottawa, Canada), fixed in alcoholic Z-fix (4% paraformaldehyde, 20% isopropyl alcohol, 2% TCA, and 2% zinc chloride), and paraffin sections (5 μm) were stained with H&E. Using digitized images of three sections traversing the optic nerve head (ONH), nuclei in rows spanning the width of the ONL were counted at 200-μm intervals superior and inferior to the ONH along the vertical meridian (0.2 to 1.6 or 2 mm) and the ONL area was calculated using a measurement interval of 0.2 mm multiplied by the sum of ONL thicknesses in superior and inferior hemiretina (ONH to 2.0 mm).

## Bisretinoid analysis in mice

Mouse eyecups (4–10 eyes/sample) were homogenized, extracted in chloroform/methanol, and concentrated as previously described (78, 79). Then the indicated mouse eyes were

## RLBP1/CRALBP gene deficiency

freeze-dried before extraction. For UPLC quantitation, murine eyecup samples were re-dissolved in ethanol after extraction and injected (10  $\mu$ l) into a Waters Acquity UPLC-MS system (Waters, Milford, MA) using an Acquity BEH Phenyl Column (1.7  $\mu$ m, 2.1  $\times$  100 mm; Waters, Milford, MA). Eluents were water/acetonitrile (1:1) with 0.1% formic acid (A) and isopropyl alcohol/acetonitrile (9:1) with 0.1% formic acid (B). Separation was achieved using the following elution gradients: 0–50 min, 100–55%; 50–110 min, 55–35%. Flow rate was 0.2 ml/min. UV absorbance peaks were identified by comparison with external standards of synthesized and purified A2E and A2GPE. Identification was confirmed by mass to charge ratio (*m/z*). Molar quantities per eye were calculated based on standard solutions with concentrations determined spectrophotometrically. Peak areas were calculated using Waters Empower Software and results were analyzed in Excel (Microsoft, Redmond WA).

For analysis by HPLC (Alliance System, Waters Corp.), samples were re-dissolved in CHCl<sub>3</sub>/MeOH = 1:1 after extraction as above and injected (30  $\mu$ l) as previously described (80). Absorbance peaks were identified using synthesized authentic compounds, and molar quantities per eye were calculated by comparison with synthesized standards. A2E and iso-A2E were measured separately and summed.

### Structural analysis

Structural figures were made in PyMOL using CRALBP crystal structure (PDB 3HY5) (81).

### Statistical analysis

*p* values were calculated using PRISM 8 (GraphPad Software).

### Data availability

All of the data are in the manuscript.

---

**Author contributions**—J. R. L. d. C., H. J. K., K. U., J. Z., A. P. O., and T. Y. investigation; J. R. L. d. C., H. J. K., K. U., J. Z., and J. R. S. writing-original draft; H. J. K., K. U., and J. Z. formal analysis; S. H. T. and J. R. S. funding acquisition; S. H. T. and J. R. S. project administration; J. R. S. conceptualization; J. R. S. writing-review and editing.

---

### References

1. Saari, J. C., Nawrot, M., Kennedy, B. N., Garwin, G. G., Hurley, J. B., Huang, J., Possin, D. E., and Crabb, J. W. (2001) Visual cycle impairment in cellular retinaldehyde binding protein (CRALBP) knockout mice results in delayed dark adaptation. *Neuron* **29**, 739–748 [CrossRef Medline](#)
2. Xue, Y., Shen, S. Q., Jui, J., Rupp, A. C., Byrne, L. C., Hattar, S., Flannery, J. G., Corbo, J. C., and Kefalov, V. J. (2015) CRALBP supports the mammalian retinal visual cycle and cone vision. *J. Clin. Invest.* **125**, 727–738 [CrossRef Medline](#)
3. Maw, M. A., Kennedy, B., Knight, A., Bridges, R., Roth, K. E., Mani, E. J., Makkadan, J. K., Nancarrow, D., Crabb, J. W., and Denton, M. J. (1997) Mutation of the gene encoding cellular retinaldehyde-binding protein in autosomal recessive retinitis pigmentosa. *Nat. Genet.* **17**, 198–200 [CrossRef Medline](#)
4. Morimura, H., Berson, E. L., and Dryja, T. P. (1999) Recessive mutations in the RLBP1 gene encoding cellular retinaldehyde-binding protein in a form of retinitis punctata albescens. *Invest. Ophthalmol. Vis. Sci.* **40**, 1000–1004 [Medline](#)
5. Eichers, E. R., Green, J. S., Stockton, D. W., Jackman, C. S., Whelan, J., McNamara, J. A., Johnson, G. J., Lupski, J. R., and Katsanis, N. (2002) Newfoundland rod-cone dystrophy, an early-onset retinal dystrophy, is caused by splice-junction mutations in RLBP1. *Am. J. Hum. Genet.* **70**, 955–964 [CrossRef Medline](#)
6. Katsanis, N., Shroyer, N. F., Lewis, R. A., Cavender, J. C., Al-Rajhi, A. A., Jabak, M., and Lupski, J. R. (2001) Fundus albipunctatus and retinitis punctata albescens in a pedigree with an R150Q mutation in RLBP1. *Clin. Genet.* **59**, 424–429 [CrossRef Medline](#)
7. Burstedt, M. S., Sandgren, O., Holmgren, G., and Forsman-Semb, K. (1999) Bothnia dystrophy caused by mutations in the cellular retinaldehyde-binding protein gene (RLBP1) on chromosome 15q26. *Invest. Ophthalmol. Vis. Sci.* **40**, 995–1000 [Medline](#)
8. Hipp, S., Zobor, G., Glöckle, N., Mohr, J., Kohl, S., Zrenner, E., Weisschuh, N., and Zobor, D. (2015) Phenotype variations of retinal dystrophies caused by mutations in the RLBP1 gene. *Acta Ophthalmol.* **93**, e281–286 [CrossRef Medline](#)
9. Burstedt, M. S., Forsman-Semb, K., Golovleva, I., Janunger, T., Wachtmeister, L., and Sandgren, O. (2001) Ocular phenotype of bothnia dystrophy, an autosomal recessive retinitis pigmentosa associated with an R234W mutation in the RLBP1 gene. *Arch. Ophthalmol.* **119**, 260–267 [Medline](#)
10. Bagheri, S., Pantrangi, M., Sodhi, S. K., Bagheri, S., Oellers, P., and Scholl, H. P. N. (2020) A novel large homozygous deletion in the cellular retinaldehyde-binding protein gene (*Rlbp1*) in a patient with retinitis punctata albescens. *Retin. Cases Brief Rep.* **14**, 85–89 [Medline](#)
11. Dessalces, E., Bocquet, B., Bourien, J., Zanlonghi, X., Verdet, R., Meunier, I., and Hamel, C. P. (2013) Early-onset foveal involvement in retinitis punctata albescens with mutations in RLBP1. *JAMA Ophthalmol.* **131**, 1314–1323 [CrossRef Medline](#)
12. Genead, M. A., Fishman, G. A., and Lindeman, M. (2010) Spectral-domain optical coherence tomography and fundus autofluorescence characteristics in patients with fundus albipunctatus and retinitis punctata albescens. *Ophthalmic. Genet.* **31**, 66–72 [CrossRef Medline](#)
13. Bocquet, B., Lacroux, A., Surget, M. O., Baudoin, C., Marquette, V., Manes, G., Hebrard, M., Sénéchal, A., Delettre, C., Roux, A. F., Claustres, M., Dhaenens, C. M., Rozet, J. M., Perrault, I., Bonnefont, J. P., Kaplan, J., et al. (2013) Relative frequencies of inherited retinal dystrophies and optic neuropathies in Southern France: assessment of 21-year data management. *Ophthalmic. Epidemiol.* **20**, 13–25 [CrossRef Medline](#)
14. Berson, E. L. (1993) Retinitis pigmentosa: the Friedenwald lecture. *Invest. Ophthalmol. Vis. Sci.* **34**, 1659–1676 [Medline](#)
15. Wang, J. S., and Kefalov, V. J. (2011) The cone-specific visual cycle. *Prog. Retin. Eye Res.* **30**, 115–128 [CrossRef Medline](#)
16. Saari, J. C. (2016) Vitamin A and vision. *Subcell. Biochem.* **81**, 231–259 [CrossRef Medline](#)
17. Sato, S., and Kefalov, V. J. (2016) cis-Retinal oxidation regulates photoreceptor access to the retina visual cycle and cone pigment regeneration. *J. Physiol.* **594**, 6753–6765 [CrossRef Medline](#)
18. Saari, J. C., and Crabb, J. W. (2005) Focus on molecules: cellular retinaldehyde-binding protein (CRALBP). *Exp. Eye Res.* **81**, 245–246 [CrossRef Medline](#)
19. Stecher, H., Gelb, M. H., Saari, J. C., and Palczewski, K. (1999) Preferential release of 11-*cis*-retinol from retinal pigment epithelial cells in the presence of cellular retinaldehyde-binding protein. *J. Biol. Chem.* **274**, 8577–8585 [CrossRef Medline](#)
20. Saari, J. C., and Bredberg, L. (1982) Enzymatic reduction of 11-*cis*-retinal bound to cellular retinal-binding protein. *Biochim. Biophys. Acta* **716**, 266–272 [CrossRef Medline](#)
21. Parker, R., Wang, J. S., Kefalov, V. J., and Crouch, R. K. (2011) Interphotoreceptor retinoid-binding protein as the physiologically relevant carrier of 11-*cis*-retinol in the cone visual cycle. *J. Neurosci.* **31**, 4714–4719 [CrossRef Medline](#)
22. Saari, J. C., and Bredberg, D. L. (1987) Photochemistry and stereoselectivity of cellular retinaldehyde-binding protein from bovine retina. *J. Biol. Chem.* **262**, 7618–7622 [Medline](#)
23. He, X., Lobsiger, J., and Stocker, A. (2009) Bothnia dystrophy is caused by domino-like rearrangements in cellular retinaldehyde-binding protein

- mutant R234W. *Proc. Natl. Acad. Sci. U.S.A.* **106**, 18545–18550 [CrossRef Medline](#)
24. von Lintig, J., Kiser, P. D., Golczak, M., and Palczewski, K. (2010) The biochemical and structural basis for trans-to-cis isomerization of retinoids in the chemistry of vision. *Trends Biochem. Sci.* **35**, 400–410 [CrossRef Medline](#)
  25. Lee, H., Deignan, J. L., Dorrani, N., Strom, S. P., Kantarci, S., Quintero-Rivera, F., Das, K., Toy, T., Harry, B., Yourshaw, M., Fox, M., Fogel, B. L., Martinez-Agosto, J. A., Wong, D. A., Chang, V. Y., *et al.* (2014) Clinical exome sequencing for genetic identification of rare Mendelian disorders. *JAMA* **312**, 1880–1887 [CrossRef Medline](#)
  26. Chen, L., Lee, W., de Carvalho, J. R. L., Jr., Chang, S., Tsang, S. H., Allikmets, R., and Sparrow, J. R. (2019) Multi-platform imaging in ABCA4-associated disease. *Sci. Rep.* **9**, 6436 [CrossRef Medline](#)
  27. Keilhauer, C. N., and Delori, F. C. (2006) Near-infrared autofluorescence imaging of the fundus: visualization of ocular melanin. *Invest. Ophthalmol. Vis. Sci.* **47**, 3556–3564 [CrossRef Medline](#)
  28. Kellner, S., Kellner, U., Weber, B. H., Fiebig, B., Weinitz, S., and Ruether, K. (2009) Lipofuscin- and melanin-related fundus autofluorescence in patients with ABCA4-associated retinal dystrophies. *Am. J. Ophthalmol.* **147**, 895–902 [CrossRef Medline](#)
  29. Paavo, M., Zhao, J., Kim, H. J., Lee, W., Zernant, J., Cai, C., Allikmets, R., Tsang, S. H., and Sparrow, J. R. (2018) Mutations in GPR143/OA1 and ABCA4 inform interpretations of short-wavelength and near-infrared fundus autofluorescence. *Invest. Ophthalmol. Vis. Sci.* **59**, 2459–2469 [CrossRef Medline](#)
  30. Duncker, T., Marsiglia, M., Lee, W., Zernant, J., Tsang, S. H., Allikmets, R., Greenstein, V. C., and Sparrow, J. R. (2014) Correlations amongst near-infrared and short-wavelength autofluorescence and spectral domain optical coherence tomography in recessive Stargardt disease. *Invest. Ophthalmol. Vis. Sci.* **55**, 8134–8143 [CrossRef Medline](#)
  31. Wang, J., Yoo, H. S., Obrochta, K. M., Huang, P., and Napoli, J. L. (2015) Quantitation of retinaldehyde in small biological samples using ultrahigh-performance liquid chromatography tandem mass spectrometry. *Anal. Biochem.* **484**, 162–168 [CrossRef Medline](#)
  32. Weng, J., Mata, N. L., Azarian, S. M., Tzekov, R. T., Birch, D. G., and Travis, G. H. (1999) Insights into the function of Rim protein in photoreceptors and etiology of Stargardt's disease from the phenotype in abcr knockout mice. *Cell* **98**, 13–23 [CrossRef Medline](#)
  33. Palczewski, K., Van Hooser, J. P., Garwin, G. G., Chen, J., Liou, G. I., and Saari, J. C. (1999) Kinetics of visual pigment regeneration in excised mouse eyes and in mice with a targeted disruption of the gene encoding interphotoreceptor retinoid-binding protein or arrestin. *Biochemistry* **38**, 12012–12019 [CrossRef Medline](#)
  34. Jin, M., Li, S., Moghrabi, W. N., Sun, H., and Travis, G. H. (2005) Rpe65 is the retinoid isomerase in bovine retinal pigment epithelium. *Cell* **122**, 449–459 [CrossRef Medline](#)
  35. Moiseyev, G., Chen, Y., Takahashi, Y., Wu, B. X., and Ma, J. X. (2005) RPE65 is the isomerohydrolase in the retinoid visual cycle. *Proc. Natl. Acad. Sci. U.S.A.* **102**, 12413–12418 [CrossRef Medline](#)
  36. Redmond, T. M., Poliakov, E., Yu, S., Tsai, J. Y., Lu, Z., and Gentleman, S. (2005) Mutation of key residues of RPE65 abolishes its enzymatic role as isomerohydrolase in the visual cycle. *Proc. Natl. Acad. Sci. U.S.A.* **102**, 13658–13663 [CrossRef Medline](#)
  37. Weleber, R. G., Michaelides, M., Trzupke, K. M., Stover, N. B., and Stone, E. M. (2011) The phenotype of Severe Early Childhood Onset Retinal Dystrophy (SECORD) from mutation of RPE65 and differentiation from Leber congenital amaurosis. *Invest. Ophthalmol. Vis. Sci.* **52**, 292–302 [CrossRef Medline](#)
  38. Littink, K. W., van Genderen, M. M., van Schooneveld, M. J., Visser, L., Riemsdijk, F. C., Keunen, J. E., Bakker, B., Zonneveld, M. N., den Hollander, A. I., Cremers, F. P., and van den Born, L. I. (2012) A homozygous frameshift mutation in LRAT causes retinitis punctata albescens. *Ophthalmology* **119**, 1899–1906 [CrossRef Medline](#)
  39. Redmond, T. M., Yu, S., Lee, E., Bok, D., Hamasaki, D., Chen, N., Goletz, P., Ma, J.-X., Crouch, R. K., and Pfeifer, K. (1998) Rpe65 is necessary for production of 11-cis-vitamin A in the retinal visual cycle. *Nat. Genet.* **20**, 344–351 [CrossRef Medline](#)
  40. Marchette, L. D., Thompson, D. A., Kravtsova, M., Ngansop, T. N., Mandal, M. N. A., and Kasus-Jacobi, A. (2010) Retinol dehydrogenase 12 detoxifies 4-hydroxynonenal in photoreceptor cells. *Free Radical Biol. Med.* **48**, 16–25 [CrossRef](#)
  41. Mandal, M. N., Moiseyev, G. P., Elliott, M. H., Kasus-Jacobi, A., Li, X., Chen, H., Zheng, L., Nikolaeva, O., Floyd, R. A., Ma, J. X., and Anderson, R. E. (2011)  $\alpha$ -Phenyl-*N*-tert-butylnitron (PBN) prevents light-induced degeneration of the retina by inhibiting RPE65 protein isomerohydrolase activity. *J. Biol. Chem.* **286**, 32491–32501 [CrossRef Medline](#)
  42. Li, F., Marchette, L. D., Brush, R. S., Elliott, M. H., Le, Y. Z., Henry, K. A., Anderson, A. G., Zhao, C., Sun, X., Zhang, K., and Anderson, R. E. (2009) DHA does not protect ELOVL4 transgenic mice from retinal degeneration. *Mol. Vis.* **15**, 1185–1193 [Medline](#)
  43. Radu, R. A., Yuan, Q., Hu, J., Peng, J. H., Lloyd, M., Nusinowitz, S., Bok, D., and Travis, G. H. (2008) Accelerated accumulation of lipofuscin pigments in the RPE of a mouse model for ABCA4-mediated retinal dystrophies following vitamin A supplementation. *Invest. Ophthalmol. Vis. Sci.* **49**, 3821–3829 [CrossRef Medline](#)
  44. Káldi, I., Martin, R. E., Huang, H., Brush, R. S., Morrison, K. A., and Anderson, R. E. (2003) Bright cyclic rearing protects albino mouse retina against acute light-induced apoptosis. *Mol. Vis.* **9**, 337–344 [Medline](#)
  45. Maeda, A., Maeda, T., Golczak, M., Chou, S., Desai, A., Hoppel, C. L., Matsuyama, S., and Palczewski, K. (2009) Involvement of all-trans-retinal in acute light-induced retinopathy of mice. *J. Biol. Chem.* **284**, 15173–15183 [CrossRef Medline](#)
  46. Maeda, A., Maeda, T., Imanishi, Y., Sun, W., Jastrzebska, B., Hatala, D. A., Winkens, H. J., Hofmann, K. P., Janssen, J. J., Baehr, W., Driessen, C. A., and Palczewski, K. (2006) Retinol dehydrogenase (RDH12) protects photoreceptors from light-induced degeneration in mice. *J. Biol. Chem.* **281**, 37697–37704 [CrossRef Medline](#)
  47. Andrieu-Soler, C., Aubert-Pouéssel, A., Doat, M., Picaud, S., Halhal, M., Simonutti, M., Venier-Julienne, M. C., Benoit, J. P., and Behar-Cohen, F. (2005) Intravitreal injection of PLGA microspheres encapsulating GDNF promotes the survival of photoreceptors in the rd1/rd1 mouse. *Mol. Vis.* **11**, 1002–1011 [Medline](#)
  48. Scimone, C., Donato, L., Esposito, T., Rinaldi, C., D'Angelo, R., and Sidoti, A. (2017) A novel RLBP1 gene geographical area-related mutation present in a young patient with retinitis punctata albescens. *Hum. Genomics* **11**, 18 [CrossRef Medline](#)
  49. Sparrow, J. R. (2016) Vitamin A-aldehyde adducts: AMD risk and targeted therapeutics. *Proc. Natl. Acad. Sci. U.S.A.* **113**, 4564–4569 [CrossRef Medline](#)
  50. Maiti, P., Kong, J., Kim, S. R., Sparrow, J. R., Allikmets, R., and Rando, R. R. (2006) Small molecule RPE65 antagonists limit the visual cycle and prevent lipofuscin formation. *Biochemistry* **45**, 852–860 [CrossRef](#)
  51. Golczak, M., Kuksa, V., Maeda, T., Moise, A. R., and Palczewski, K. (2005) Positively charged retinoids are potent and selective inhibitors of the trans-cis isomerization in the retinoid (visual) cycle. *Proc. Natl. Acad. Sci. U.S.A.* **102**, 8162–8167 [CrossRef Medline](#)
  52. Kiser, P. D., Zhang, J., Badiie, M., Li, Q., Shi, W., Sui, X., Golczak, M., Tochtrop, G. P., and Palczewski, K. (2015) Catalytic mechanism of a retinoid isomerase essential for vertebrate vision. *Nat. Chem. Biol.* **11**, 409–415 [CrossRef Medline](#)
  53. Bavik, C., Henry, S. H., Zhang, Y., Mitts, K., McGinn, T., Budzynski, E., Pashko, A., Lieu, K. L., Zhong, S., Blumberg, B., Kuksa, V., Orme, M., Scott, I., Fawzi, A., and Kubota, R. (2015) Visual cycle modulation as an approach toward preservation of retinal integrity. *PLoS ONE* **10**, e0124940 [CrossRef Medline](#)
  54. Maeda, A., Golczak, M., Chen, Y., Okano, K., Kohno, H., Shiose, S., Ishikawa, K., Harte, W., Palczewska, G., Maeda, T., and Palczewski, K. (2011) Primary amines protect against retinal degeneration in mouse models of retinopathies. *Nat. Chem. Biol.* **8**, 170–178 [CrossRef Medline](#)
  55. Mata, N. L., and Vogel, R. (2010) Pharmacologic treatment of atrophic age-related macular degeneration. *Curr. Opin. Ophthalmol.* **21**, 190–196 [CrossRef Medline](#)
  56. Mata, N. L., Lichter, J. B., Vogel, R., Han, Y., Bui, T. V., and Singerman, L. J. (2013) Investigation of oral fenretinide for treatment of geographic atro-

- phy in age-related macular degeneration. *Retina* **33**, 498–507 [CrossRef Medline](#)
57. Dobri, N., Qin, Q., Kong, J., Yamamoto, K., Liu, Z., Moiseyev, G., Ma, J. X., Allikmets, R., Sparrow, J. R., and Petrukhin, K. (2013) A1120, a nonretinoid RBP4 antagonist, inhibits formation of cytotoxic bisretinoids in the animal model of enhanced retinal lipofuscinogenesis. *Invest. Ophthalmol. Vis. Sci.* **54**, 85–95 [CrossRef Medline](#)
  58. Ma, L., Kaufman, Y., Zhang, J., and Washington, I. (2011) C20-D3-vitamin A slows lipofuscin accumulation and electrophysiological retinal degeneration in a mouse model of Stargardt disease. *J. Biol. Chem.* **286**, 7966–7974 [CrossRef Medline](#)
  59. Kaufman, Y., Ma, L., and Washington, I. (2011) Deuterium enrichment of vitamin A at the C20 position slows the formation of detrimental vitamin A dimers in wild-type rodents. *J. Biol. Chem.* **286**, 7958–7965 [CrossRef Medline](#)
  60. Golovleva, I., Bhattacharya, S., Wu, Z., Shaw, N., Yang, Y., Andrabi, K., West, K. A., Burstedt, M. S., Forsman, K., Holmgren, G., Sandgren, O., Noy, N., Qin, J., and Crabb, J. W. (2003) Disease-causing mutations in the cellular retinaldehyde binding protein tighten and abolish ligand interactions. *J. Biol. Chem.* **278**, 12397–12402 [CrossRef Medline](#)
  61. Wu, Z., Hasan, A., Liu, T., Teller, D. C., and Crabb, J. W. (2004) Identification of CRALBP ligand interactions by photoaffinity labeling, hydrogen/deuterium exchange, and structural modeling. *J. Biol. Chem.* **279**, 27357–27364 [CrossRef Medline](#)
  62. Wu, L., Ueda, K., Nagasaki, T., and Sparrow, J. R. (2014) Light damage in Abca4 and Rpe65rd12 mice. *Invest. Ophthalmol. Vis. Sci.* **55**, 1910–1918 [CrossRef Medline](#)
  63. Russell, S., Bennett, J., Wellman, J. A., Chung, D. C., Yu, Z. F., Tillman, A., Wittes, J., Pappas, J., Elci, O., McCague, S., Cross, D., Marshall, K. A., Walshire, J., Kehoe, T. L., Reichert, H., *et al.* (2017) Efficacy and safety of voretigene neparvovec (AAV2-hRPE65v2) in patients with RPE65-mediated inherited retinal dystrophy: a randomised, controlled, open-label, phase 3 trial. *Lancet* **390**, 849–860 [CrossRef Medline](#)
  64. Jacobson, S. G., Cideciyan, A. V., Roman, A. J., Sumaroka, A., Schwartz, S. B., Heon, E., and Hauswirth, W. W. (2015) Improvement and decline in vision with gene therapy in childhood blindness. *N. Engl. J. Med.* **372**, 1920–1926 [CrossRef Medline](#)
  65. Kumaran, N., Michaelides, M., Smith, A. J., Ali, R. R., and Bainbridge, J. W. B. (2018) Retinal gene therapy. *Br. Med. Bull.* **126**, 13–25 [CrossRef Medline](#)
  66. Choi, V. W., Bigelow, C. E., McGee, T. L., Gujar, A. N., Li, H., Hanks, S. M., Vrouvlianis, J., Maker, M., Leehy, B., Zhang, Y., Aranda, J., Bounoutas, G., Demirs, J. T., Yang, J., Ornborg, R., *et al.* (2015) AAV-mediated RLBP1 gene therapy improves the rate of dark adaptation in Rlbp1 knockout mice. *Mol. Ther. Methods Clin. Dev.* **2**, 15022 [CrossRef Medline](#)
  67. MacLachlan, T. K., Milton, M. N., Turner, O., Tukov, F., Choi, V. W., Penraat, J., Delmotte, M. H., Michaut, L., Jaffee, B. D., and Bigelow, C. E. (2018) Nonclinical safety evaluation of scAAV8-RLBP1 for treatment of RLBP1 retinitis pigmentosa. *Mol. Ther. Methods Clin. Dev.* **8**, 105–120 [CrossRef Medline](#)
  68. Staurenghi, G., Sadda, S., Chakravarthy, U., Spaide, R. F., and International Nomenclature for Optical Coherence Tomography Panel (2014) Proposed lexicon for atomic landmarks in normal posterior segment spectral-domain optical coherence tomography: the IN<sup>o</sup>OCT consensus. *Ophthalmology* **121**, 1572–1578 [CrossRef Medline](#)
  69. Duncker, T., Greenberg, J. P., Ramachandran, R., Hood, D. C., Smith, R. T., Hirose, T., Woods, R. L., Tsang, S. H., Delori, F. C., and Sparrow, J. R. (2014) Quantitative fundus autofluorescence and optical coherence tomography in BEst vitelliform macular dystrophy. *Invest. Ophthalmol. Vis. Sci.* **55**, 1471–1482 [CrossRef Medline](#)
  70. Duncker, T., Stein, G. E., Lee, W., Tsang, S. H., Zernant, J., Bearely, S., Hood, D. C., Greenstein, V. C., Delori, F. C., Allikmets, R., and Sparrow, J. R. (2015) Quantitative fundus autofluorescence and optical coherence tomography in ABCA4 carriers. *Invest. Ophthalmol. Vis. Sci.* **56**, 7274–7285 [CrossRef](#)
  71. Duncker, T., Tsang, S. H., Lee, W., Zernant, J., Allikmets, R., Delori, F. C., and Sparrow, J. R. (2015) Quantitative fundus autofluorescence distinguishes ABCA4-associated and non-ABCA4-associated Bull's-Eye maculopathy. *Ophthalmology* **122**, 345–355 [CrossRef Medline](#)
  72. Duncker, T., Tsang, S. H., Woods, R. L., Lee, W., Zernant, J., Allikmets, R., Delori, F. C., and Sparrow, J. R. (2015) Quantitative fundus autofluorescence and optical coherence tomography in PRPH2/RDS- and ABCA4-associated disease exhibiting phenotypic overlap. *Invest. Ophthalmol. Vis. Sci.* **56**, 3159–3170 [CrossRef Medline](#)
  73. van de Kraats, J., and van Norren, D. (2007) Optical density of the aging human ocular media in the visible and the UV. *J. Opt. Soc. Am. A Opt. Image. Sci. Vis.* **24**, 1842–1857 [CrossRef Medline](#)
  74. Greenberg, J. P., Duncker, T., Woods, R. L., Smith, R. T., Sparrow, J. R., and Delori, F. C. (2013) Quantitative fundus autofluorescence in healthy eyes. *Invest. Ophthalmol. Vis. Sci.* **54**, 5684–5693 [CrossRef Medline](#)
  75. Sparrow, J. R., Blonska, A., Flynn, E., Duncker, T., Greenberg, J. P., Secondi, R., Ueda, K., and Delori, F. C. (2013) Quantitative fundus autofluorescence in mice: correlation with HPLC quantitation of RPE lipofuscin and measurement of retina outer nuclear layer thickness. *Invest. Ophthalmol. Vis. Sci.* **54**, 2812–2820 [CrossRef Medline](#)
  76. Flynn, E., Ueda, K., Auran, E., Sullivan, J. M., and Sparrow, J. R. (2014) Fundus autofluorescence and photoreceptor cell rosettes in mouse models. *Invest. Ophthalmol. Vis. Sci.* **55**, 5643–5652 [CrossRef Medline](#)
  77. Zhao, J., Ueda, K., Riera, M., Kim, H. J., and Sparrow, J. R. (2018) Bisretinoids mediate light sensitivity resulting in photoreceptor cell degeneration in mice lacking the receptor tyrosine kinase Mer. *J. Biol. Chem.* **293**, 19400–19410 [CrossRef Medline](#)
  78. Yamamoto, K., Yoon, K. D., Ueda, K., Hashimoto, M., and Sparrow, J. R. (2011) A novel bisretinoid of retina is an adduct on glycerophosphoethanolamine. *Invest. Ophthalmol. Vis. Sci.* **52**, 9084–9090 [CrossRef Medline](#)
  79. Wu, Y., Fishkin, N. E., Pande, A., Pande, J., and Sparrow, J. R. (2009) Novel lipofuscin bisretinoids prominent in human retina and in a model of recessive Stargardt disease. *J. Biol. Chem.* **284**, 20155–20166 [CrossRef Medline](#)
  80. Ueda, K., Zhao, J., Kim, H. J., and Sparrow, J. R. (2016) Photodegradation of retinal bisretinoids in mouse models and implications for macular degeneration. *Proc. Natl. Acad. Sci.* **113**, 6904–6909 [CrossRef Medline](#)
  81. Stocker, A., He, X., Lobisger, J. (2009) Crystal Structure of CRALBP. Protein Data Bank, 3HY5.